Supplementary Information

Electric double layer overlapping effect in high-density sub-nanoclusters for enhanced acidic oxygen evolution reaction

Jiahui Yang[1], Yixin Hao[2], Liming Deng[2], Sung-Fu Hung[3], Luqi Wang[2], Gengyu Xing[2], Feng Hu[2], Linlin Li[2]*, Tao Wang[1]*, Jianwei Ren[4], Yuping Wu[1], Shengjie Peng[1]*

[1]Confucius Energy Storage Lab, School of Energy and Environment & Z Energy Storage Center, Southeast University, Nanjing 211189, China.
[2]College of Materials Science and Technology, Nanjing University of Aeronautics and Astronautics, Nanjing 210016, China.
[3]Department of Applied Chemistry, National Yang Ming Chiao Tung University, Hsinchu 300, Taiwan.
[4]Department of Chemical Engineering, University of Pretoria, Pretoria 0028, South Africa.

This PDF file includes:

1. Experimental Section

1.1 Chemicals.

Ruthenium (III) chloride trihydrate ($RuCl_3 \cdot 3H_2O$), commercial h-BN (parent bulk h-BN, lateral size 1 mm) powder, and RuO_2 (99.9% trace metals basis) were purchased from Macklin. KOH, NaOH, and isopropanol were purchased from Sigma-Aldrich (Shanghai, China). All of the above chemicals were analytical grade and used as received without further purification.

1.2 Materials preparation.

Preparation of BNC. A mixture of boric acid and urea with a fixed mass ratio (0.1 g H_3BO_3 and 3 g urea) was dissolved in a solvent composed of deionized water (5 mL) and ethanol (5 mL), followed by the addition of polyethylene-polypropylene glycol (F127) (0.2 g). The mixture in a glass vial was stirred vigorously on a magnetic stirrer until complete dissolution. The resulting solution was then heated at 80 °C under stirring to allow recrystallization. After evaporation of the solvent, a white crystalline powder was obtained, which was ground thoroughly in a mortar to remove any large particles. The powder was subsequently calcined at 800 °C for 120 minutes under an Ar atmosphere in a tube furnace, yielding a black powder product denoted as BNC.

Preparation of RuO_2-SCs/BNC. First, 30 mg of BNC powder and 30 mg of $RuCl_3$ were uniformly dispersed in 30 mL of deionized water to form a mixed solution. The resulting mixture was frozen using liquid nitrogen and then freeze-dried under vacuum for 72 hours. The obtained black powder was finally calcined in a muffle furnace at 350 °C for 4 hours in air to obtain RuO_2-SCs/BNC.

Preparation of RuO_2-NPs/BNC. A total of 30 mg of BNC powder and 30 mg of $RuCl_3$ were uniformly dispersed in 30 mL of deionized water. The mixture was sonicated until complete dissolution of $RuCl_3$, followed by adjusting the pH to neutral using 1 mol/L NaOH solution. The mixture was stirred at room temperature for 12 hours. The resulting suspension was centrifuged and washed, and the solid product was collected and dried overnight in a vacuum oven at 60 ℃. The dried powder was calcined in a muffle furnace at 350 °C for 4 hours in air to obtain RuO_2-NPs/BNC.

1.3 Materials Characterization.

General characterizations: The morphologies of catalysts were observed by SEM (SEM, JEOL JSM-6700 F), HR-TEM (TEM-EDX, Philips Tecnai F20, 200 kV), and aberration-corrected transmission electron microscope (ACTEM, JEOL JEM-ARM200F). The elemental compositions were analyzed by ICP (ICP-OES, inductively coupled plasma optical emission spectroscopy). The crystal structure of the samples was characterized by X-ray powder diffraction (XRD, Bruker D8 Discover) with Cu Kα radiation (λ = 1.5418 Å). The chemical valence state and surface atomic ratio were collected by X-ray photoelectron spectroscopy (XPS, ESCALAB 250Xi). The extended X-ray absorption fine structure (EXAFS) was measured at Taiwan Photon Source (TPS) beamline, 44A Quick-scanning X-ray absorption spectroscopy (XAS), in National

Synchrotron Radiation Research Center (NSRRC), Hsinchu, Taiwan. The Electron paramagnetic resonance (EPR, Bruker EMX-6/1) was used to obtain information about the vacancy concentration. Resonance Raman spectra were conducted on a confocal Raman microscope (Invia Reflex) with 532 nm wavelength at the sample surface.

In situ ATR-SEIRAS experiment. A Nicolet iS50 FT-IR spectrometer with a liquid nitrogen-cooled MCT detector and a fixed-angle IR optical path performed ATR-SEIRAS measurements. The spectral resolution of the measurements was 8 cm^{-1} and 32 interferograms were added for each spectrum. The working electrode was prepared in two main steps: first, an ultra-thin Au film was chemically deposited on a silicon crystal to enhance the IR signal and facilitate electron conduction; second, a catalyst slurry was drop-cast onto the Au surface with a loading of 0.1 mg cm^{-2}. The catalyst slurry was prepared as follows: 7 mg of catalyst and 3 mg of carbon black were dispersed in 1 mL of ethanol, followed by the addition of 50 μL of Nafion (sonicated for 30 min). The prepared working electrodes were mounted in an electrochemical three-electrode cell with Ag/AgCl as the reference electrode, Pt foil as the counter electrode, and Ar-saturated 0.5 M H_2SO_4 as the electrolyte for the OER reaction. All measurements were carried out using linear scanning voltammetry (LSV) to analyze the OER reaction intermediates at different potentials, respectively.

In situ Raman measurements. A micro-confocal Raman spectroscopy system was constructed using the SmartRaman microconfocal module and the HORIBA iHR550 spectrometer, equipped with a 50x long focal microscope objective. In situ Raman spectroscopy measurements were conducted in a custom flow-type in situ Raman electrolytic cell. Before the experiments, the Raman spectroscopy system was calibrated using a standard silicon wafer (520.7 cm^{-1}) with a laser wavelength of 532 nm.

In situ EIS measurements. In situ characterization tandem electrochemical operation was carried out at the specified potential to obtain the surface chemical composition and structural information of the materials. EIS tests were performed at different potentials in the frequency range of 0.01 - 100,000 Hz.

In situ XAFS measurements. In-situ X-ray absorption spectroscopy, including XANES and EXAFS at Ru K-edge, was collected in total-fluorescence-yield mode using a silicon drift detector in BL-44A at National Synchrotron Radiation Research Centre (NSRRC), Taiwan. The measurement in a typical three-electrode setup under the same conditions as the electrochemical characterization case was performed in a specially designed Teflon container with a window sealed by Kepton tape. The scan range was kept in an energy range of 21900-22800 eV for Ru K-edge. Subtracting the baseline of pre-edge and normalizing that of post-edge obtained the spectra. EXAFS analysis was conducted using a Fourier transform on k2-weighted EXAFS oscillations. All EXAFS spectra are presented without phase correction.

2. Electrochemical Measurement

2.1 Electrochemical experiments in a three-electrode setup

Electrochemical measurements were performed in a three-electrode system at room

temperature using an Autolab PGSTAT302 electrochemical workstation. The electrolyte was a 0.5 M H_2SO_4 solution saturated with argon. The working electrodes were prepared as follows.

For the RuO_2-SCs/BNC working electrode, 7 mg of RuO_2-SCs/BNC electrocatalyst, 2 mg of carbon black, and 1 mg of polyvinylidene fluoride (PVDF) binder were weighed and then mixed in 2 mL of N-methyl-2-pyrrolidone (NMP) solvent to form a uniform slurry. For the RuO_2-NPs/BNC working electrode, 7 mg of RuO_2-NPs/BNC electrocatalyst, 2 mg of carbon black, and 1 mg of PVDF binder were weighed and then mixed in 2 mL of NMP solvent to form a uniform slurry. For the RuO_2 working electrode, 2.1 mg commercial RuO_2, 0.6 mg of carbon black and 0.3 mg of PVDF binder were weighed and then mixed in 2 mL of NMP solvent to form a uniform slurry. For the BNC working electrode, 4.9 mg of BNC, 1.4 mg of carbon black and 0.7 mg of PVDF binder were weighed and then mixed in 2 mL of NMP solvent to form a uniform slurry. The as-prepared slurries were individually subjected to ultrasonication for 2 h to ensure homogeneous dispersion. Subsequently, 500 μL of each slurry was uniformly drop-cast onto a 1 cm^2 carbon paper substrate and dried under infrared irradiation to obtain the working electrodes, with a RuO_2 loading of ~ 0.5 mg cm^{-2} for each sample.

A platinum plate was used as the counter electrode, and an Hg/ H_2SO_4 electrode (saturated with 0.5 M H_2SO_4) served as the reference electrode. All of the potentials were referenced to a reversible hydrogen electrode (RHE) according to the Nernst equation ($E_{RHE} = E_{Hg/H2SO4} + 0.682\ V + 0.0591 \times pH$). The pH of the electrolyte, 0.30 ± 0.01, was measured using a pH-meter (Mettler Toledo, Germany) before each electrochemical test. Polarization curves were measured by linear sweep voltammetry (LSV) at a scan rate of 5 mV s^{-1} and compensated using iR. Manual post-correction for ohmic drop was applied using the formula $E = E_{applied} - iR$, where i is the current flowing through the cell, and R is the ohmic resistance of the cell. Cyclic voltammograms (CV) were recorded at increasing scan rates (20-100 mV s^{-1}) to obtain electrochemical surface area (ECSA). Electrochemical impedance spectroscopy (EIS) was carried out at a potential of open circuit voltage vs. RHE with frequencies from 0.01 Hz to 100 kHz with an amplitude of 5 mV. The double-layer capacitance (C_{dl}) was obtained by collecting CV curves with scan rates of 20 to 100 mV s^{-1}.

2.2 Pulse voltammetry (PV)

Pulse voltammetry was performed while following current over time (1,600 rpm RDE). The potential was kept at a low potential (E_l = 1.15 V vs. Ag/AgCl), then switched and kept at a higher potential (E_h) before returning to El. This cycle was repeated while increasing E_h from 1.22 V to 1.30 V in 20 mV/step and keeping E_l unchanged. The charge related to the potential step was calculated by integrating the current pulse over time, accounting for the background current signal.

2.3 MEA fabrication and PEMWE electrolyzer tests

A Nafion 117 membrane was sequentially washed by 5 wt% H_2O_2, Milli-Q water and 0.5 M H_2SO_4, for 1 hour each to effectively remove contaminants from the

membrane and promote protonation of the sulfonic acid groups. The treated membrane was preserved in a 0.5 M H_2SO_4 electrolyte. The membrane electrode assembly was prepared using Nafion 117 by the catalyst-coated membrane method with a geometric area of 2 cm × 2 cm (4 cm^2). The commercial Pt/C (20 wt%) was used as the cathode for the hydrogen evolution reaction, and the RuO_2-SCs/BNC electrocatalyst was used as the anode for the oxygen evolution reaction. To prepare the anodic catalyst ink, 10 mg of the RuO_2-SCs/BNC electrocatalyst powder was suspended in a mixture of 940 μL ethanol and 60 μL Nafion (5 wt%) and was sonicated for at least 2 h. The mass loadings of the RuO_2-SCs/BNC powder were 2.5 mg cm^{-2} for the anode. The mass loadings of Pt/C (20%) were 0.2 mg_{pt} cm^{-2} for the cathode. The sprayed membrane, anode gas diffusion layer (Ti felt), and cathode gas diffusion layer (carbon paper) were hot-pressed to establish the MEA at 125°C with a pressure of 2 MPa for 3 min. The anode and cathode plates were heated to 80°C during the test. Besides, a flow of water preheated to 80°C at 150 mL min^{-1} was supplied to the anode side. The performance evaluation of the PEMWE using the RuO_2-SCs/BNC || Pt/C electrocatalyst was performed by an ITECH, IT-M3223 device. The I-V curve was collected at a scan rate of 5 mV s^{-1}, typically between 1.2 and 1.85 V.

2.4 Calculation of the specific current density per electrochemically active surface area (ECSA).

The electrochemical double-layer capacitance (C_{dl}) was determined by measuring the capacitive current associated with double-layer charging from the scan-rate dependence of cyclic voltammetry stripping. The C_{dl} was estimated by plotting the $\Delta j = (j_a - j_c)$, where j_c and j_a are the cathodic and anodic current densities, respectively, against the scan rate, in which the slope was twice that of C_{dl}.

2.5 Calculation of the turnover frequency (TOF)

The turnover frequency of the catalysts was calculated using following equation:

$$TOF(h^{-1}) = 3600 \times TOF(S^{-1}) = 3600 \times \frac{Total\ oxygen\ turnovers\ per\ A_{geo}}{Active\ sites\ per\ A_{geo}}$$

The turnover per geometric area was obtained from the geometric current density for the LSV polarization curves according to the equation:

$$Oxygen\ turnover\ per\ A_{geo} = j_{geo} \times \frac{1\ C\ s^{-1}}{1000\ mA} \times \frac{1\ mol}{96485.3\ C} \times \frac{1}{4} \times \frac{6.023 \times 10^{23}}{1\ mol\ O_2}$$

All Ru atoms were assumed to be active sites. Therefore, the number of active sites per geometric area equals the number of Ru atoms per geometric area, which can be calculated from the results of the ICP-OES analysis.

2.6 Calculation of the specific activity

The specific current density per ECSA (j_s) was calculated as shown in equation:

$$j_s = \frac{j_{geo}}{ECSA}$$

where j_{geo} is the geometric current density.

3. Computational Calculations

3.1 COMSOL Multiphysics

The modelling of the ion accumulation-diffusion process was performed in COMSOL Multiphysics software with the diluted species transport module and the electrical module. First, three different models were constructed: RuO_2 particle diameters of 1.4 nm, with spacing distributions between each particle set at 0.4 nm, 1.4 nm, and 2.4 nm. For simplicity, each model uses the same number of particles (4 particles). Then, a computational domain is used to enclose these four particles, ensuring that the particles in each model are within the range of the electric field calculation.

And the electroneutrality assumption was represented as

$$F\sum_{i=1}^{n} z_i c_i = 0$$

Based on the steady-state continuity equations and the law of mass conservation, we have

$$\frac{\partial_{c_i}}{\partial_t} + \nabla . N_i = 0$$

The boundary condition was set as followed:

$$\vec{n} \cdot J = 0$$

where J means the species flux on the boundary face.

The control equations for electrochemical reactions and concentration distribution are as follows：

$$\frac{\partial_{c_i}}{\partial_t} + \nabla . j_i + \mathrm{u}\, \nabla . c_i = R_i$$

It can be seen that electrochemical reactions act as source terms, providing reactants to the diffusion equation. The reaction rate follows the Arrhenius reaction formula:

$$R = Ae^{-E_a/RT}$$

In the equation, c is the concentration, J represents the flux of diffusion, R is the reaction rate, k is the rate constant; A is the characteristic constant of the given reaction, known as the pre-exponential factor; e is the base of natural logarithm (2.718); R is the gas constant (8.314 $J \cdot mol^{-1} \cdot K^{-1}$), E_α is the activation energy of the reaction.

Due to the different shapes and surface reaction coefficients of the two materials, different reactant concentrations can be obtained.

For the sake of simplifying the simulation model, the conductivity within the calculation domain was set to 231[mS cm^{-1}]. At the bulk domain, a uniform

concentration was assumed to be equal to the bulk concentration, where the products have the initial concentration of 0 mol/m^3. The bottom surface of the bulk domain was applied with a 1.4 V electric potential. And ions were generated from the surface of the catalyst.

The Debye length (λ_D) of the system containing RuO_2 particles (with a diameter of 1.4 nm and an interparticle spacing of 0.4 nm) was calculated using the following equation:

$$\lambda_D = \sqrt{\frac{\varepsilon_0 \cdot k_B \cdot T_e}{n_e \cdot e^2}}$$

where ε_0 means vacuum electric permeability, k_B means Boltzmann constant, T_e means electron temperature, n_e means electron density, e means elementary charge.

3.2 DFT

All DFT calculations were performed using the Vienna Ab initio Simulation Package (VASP). The projector augmented wave (PAW) pseudopotential with the PBE generalized gradient approximation (GGA) exchange correlation function was utilized in the computations. All energetics of metal oxides were calculated using the DFT with the Hubbard-U framework (DFT+U) to account for strongly localized d-electrons for Ru. The Hubbard-U correction terms were at U_{eff} = 3.32 eV as obtained via linear response theory. The cutoff energy of the plane wave basis set was 500 eV, and a Monkhorst-Pack mesh of 3×3×1 was used in K-sampling. All structures were spin polarized and all atoms were fully relaxed with the energy convergence tolerance of 10^{-5} eV per atom, and the final force on each atom was < 0.05 eV Å^{-1}.

Figures and tables

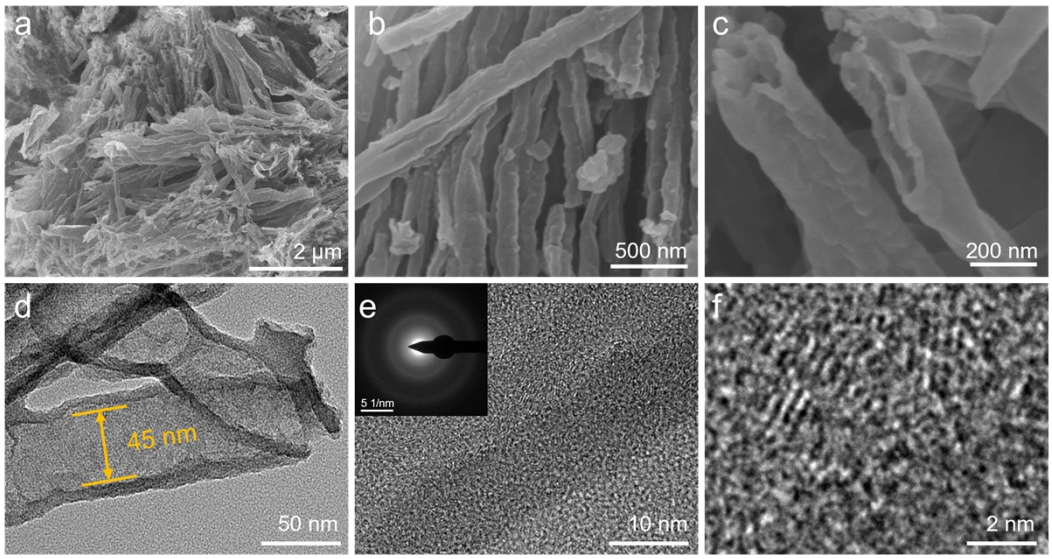

Figure S1. (a-c) SEM images, (d-f) TEM images of the BNC nanotube from low to high resolution. Inset in Figure 13e shows the corresponding SAED pattern of the BNC nanotube.

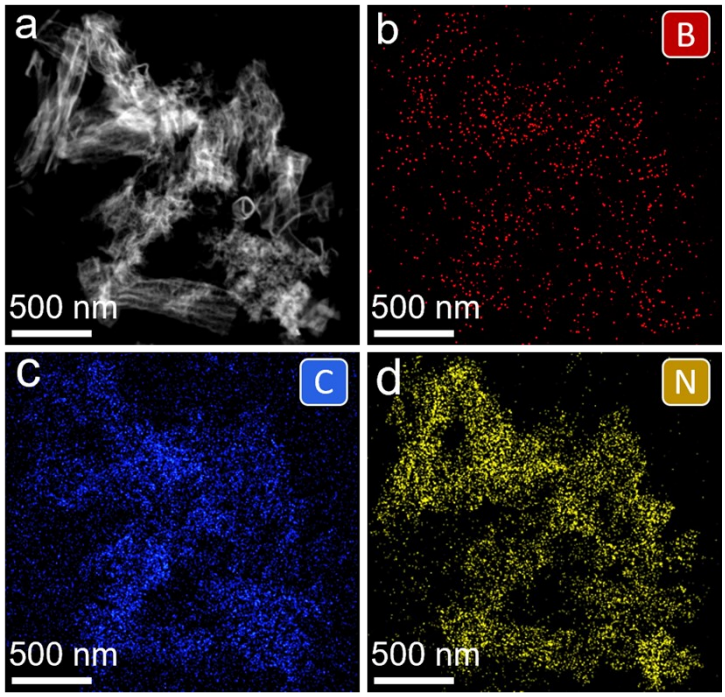

Figure S2. (a) A TEM image of the BNC nanotube and (b-d) corresponding element mappings of B, C, and N.

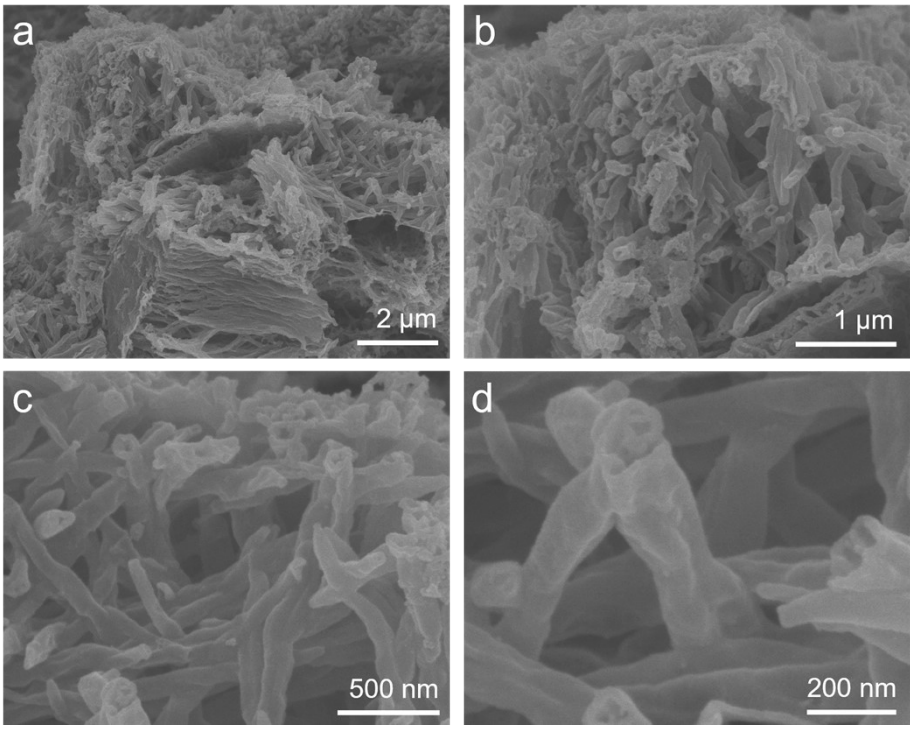

Figure S3. SEM images of RuO_2-SCs/BNC from low to high resolution. (a) 2 μm, (b) 1 μm, (c) 500 nm, (d) 200 nm.

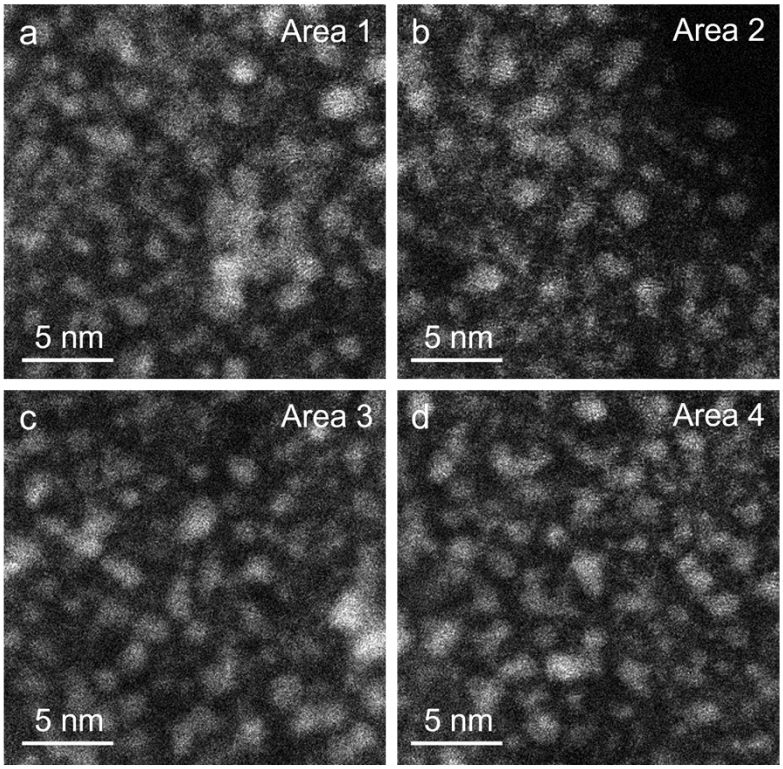

Figure S4. (a-d) AC HAADF-STEM images of RuO_2-SCs/BNC selected from four different areas randomly.

To fully illustrate that RuO_2-SCs were uniformly distributed on the BNC support, we randomly selected four regions, as shown in the figure above, which clearly showed that the size and spatial distribution of RuO_2-SCs were uniform.

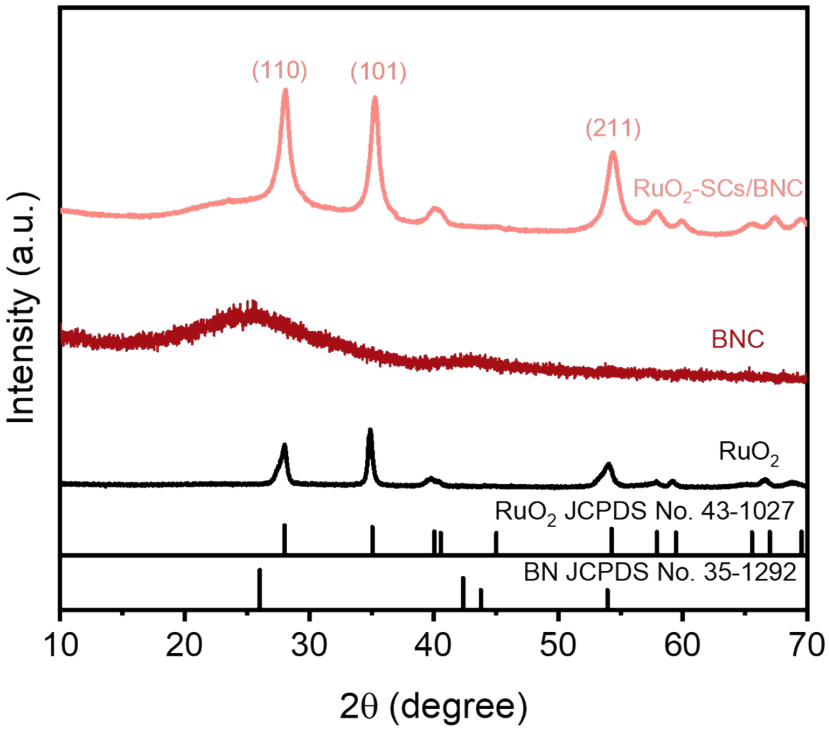

Figure S5. XRD patterns of BNC, RuO_2 and RuO_2-SCs/BNC, respectively.

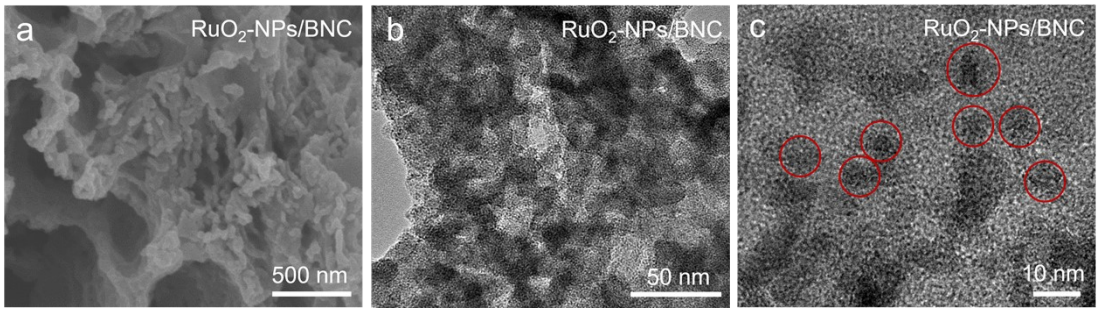

Figure S6. (a) SEM image, (b, c) TEM images of RuO_2-NPs/BNC.

The red circles marked in Figure S7c suggested the size of RuO_2-NPs loaded on BNC support is around 10 nm, which is much larger than RuO_2-SCs. This indicated that when the mass of RuO_2 loaded on the BNC support was controlled to be the same, the edge-to-edge distance of RuO_2-NPs would increase significantly compared with that of RuO_2-SCs, resulting in the disappearance of the EDL overlapping effect.

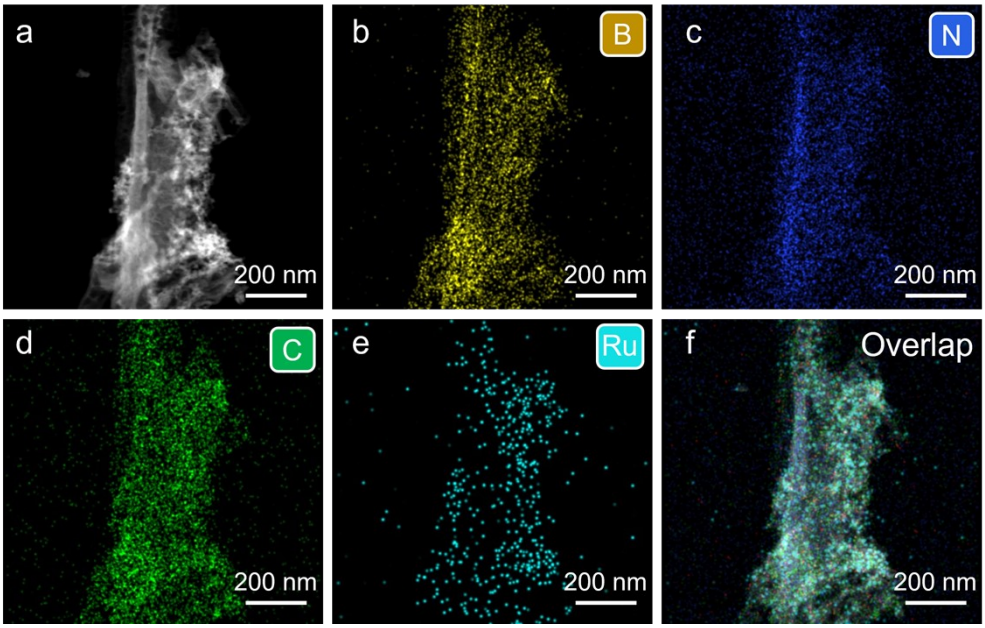

Figure S7. (a) A TEM image and (b-f) corresponding element mapping images of RuO_2-NPs/BNC.

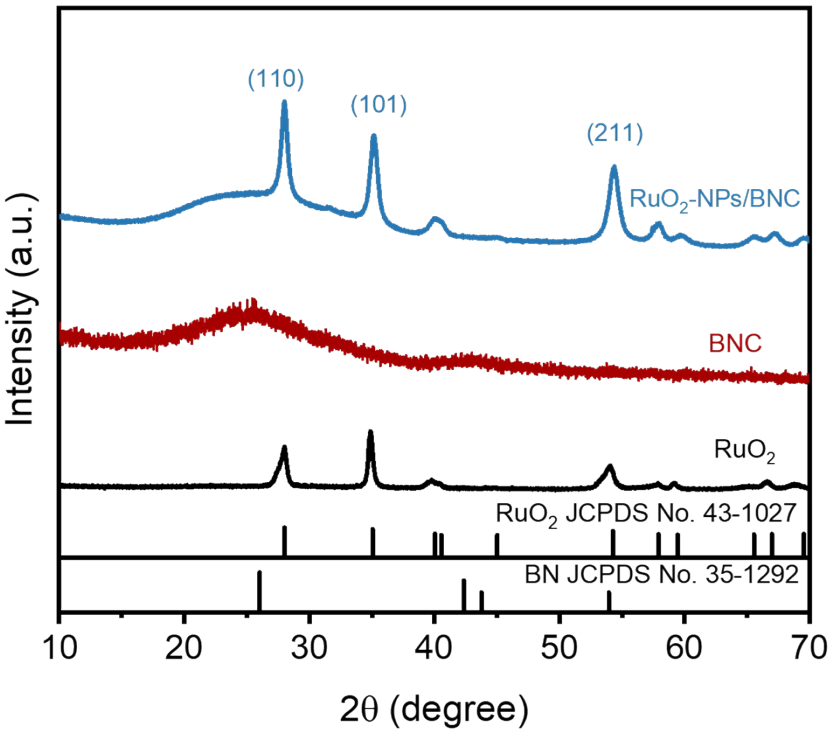

Figure S8. XRD patterns of BNC, RuO_2 and RuO_2-NPs/BNC, respectively.

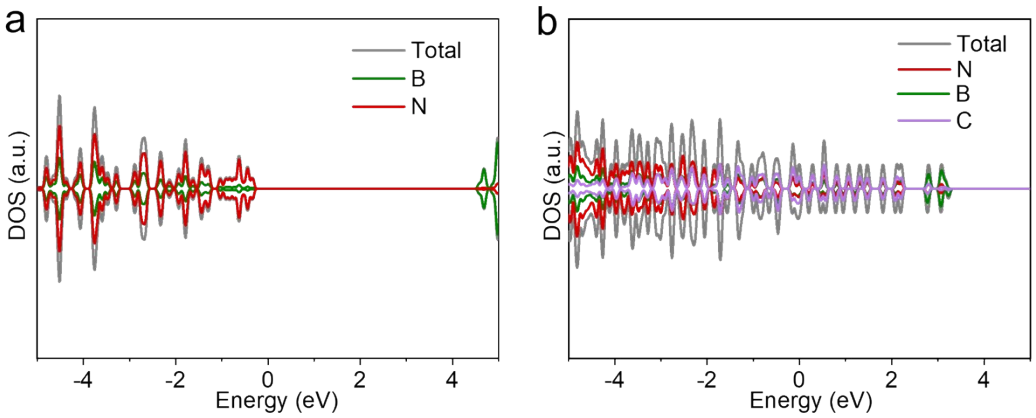

Figure S9. DOS curves for the corresponding B, N, C, O and Ru of (a)h-BN, (b) BNC.

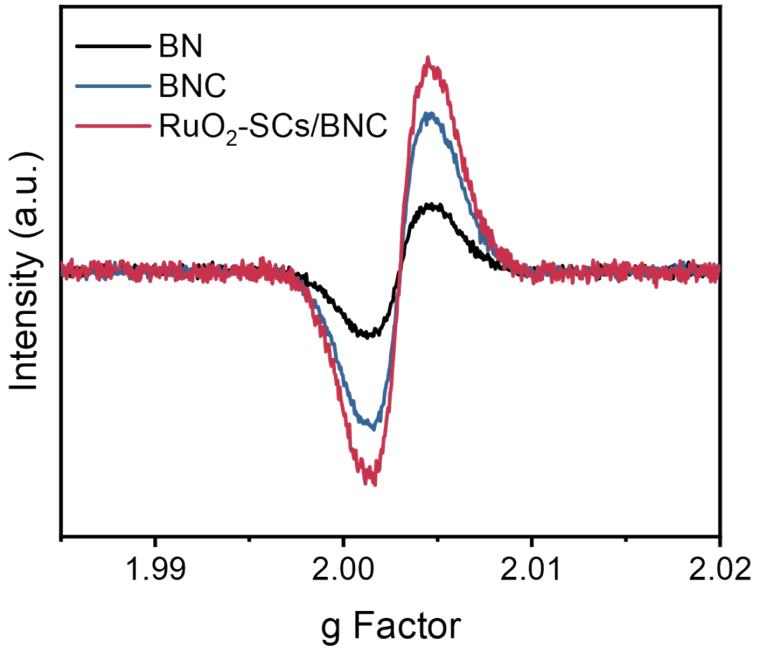

Figure S10. EPR spectra of BN, BNC and RuO_2-SCs/BNC, respectively.

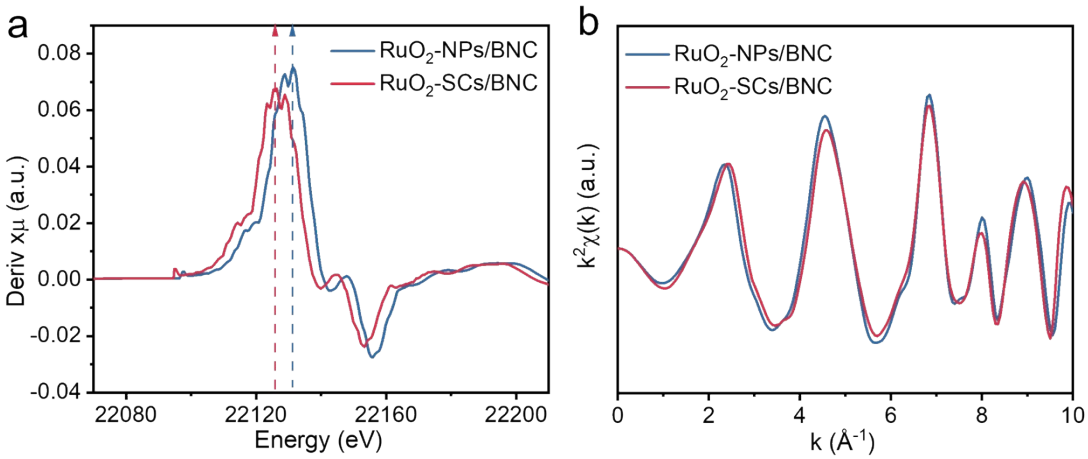

Figure S11. (a) The first derivative of Ru K-edge XANES data for RuO_2-SCs/BNC and RuO_2-NPs/BNC. (b) EXAFS oscillations of Ru K-edges for the RuO_2-SCs/BNC (red) and RuO_2-NPs/BNC (blue).

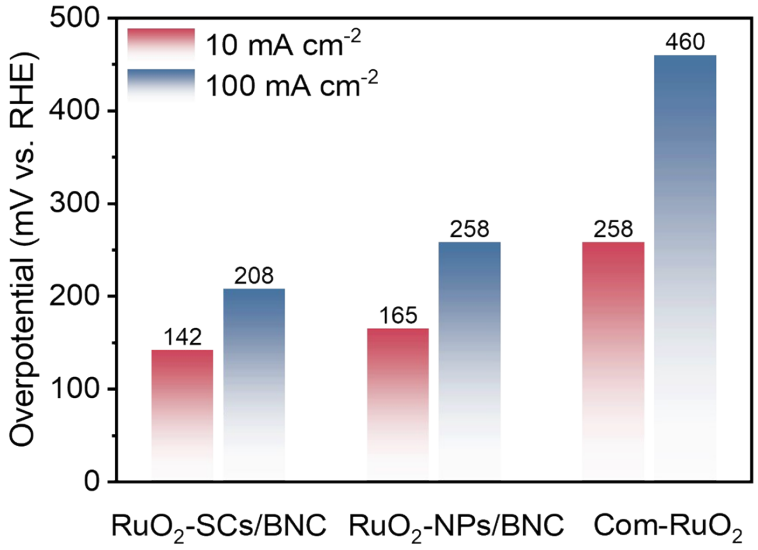

Figure S12. Overpotential histogram of commercial RuO_2, RuO_2-SCs/BNC and RuO_2-NPs/BNC at the current densities of 10 and 100 mA cm^{-2}, achieved from the iR-corrected polarization curves.

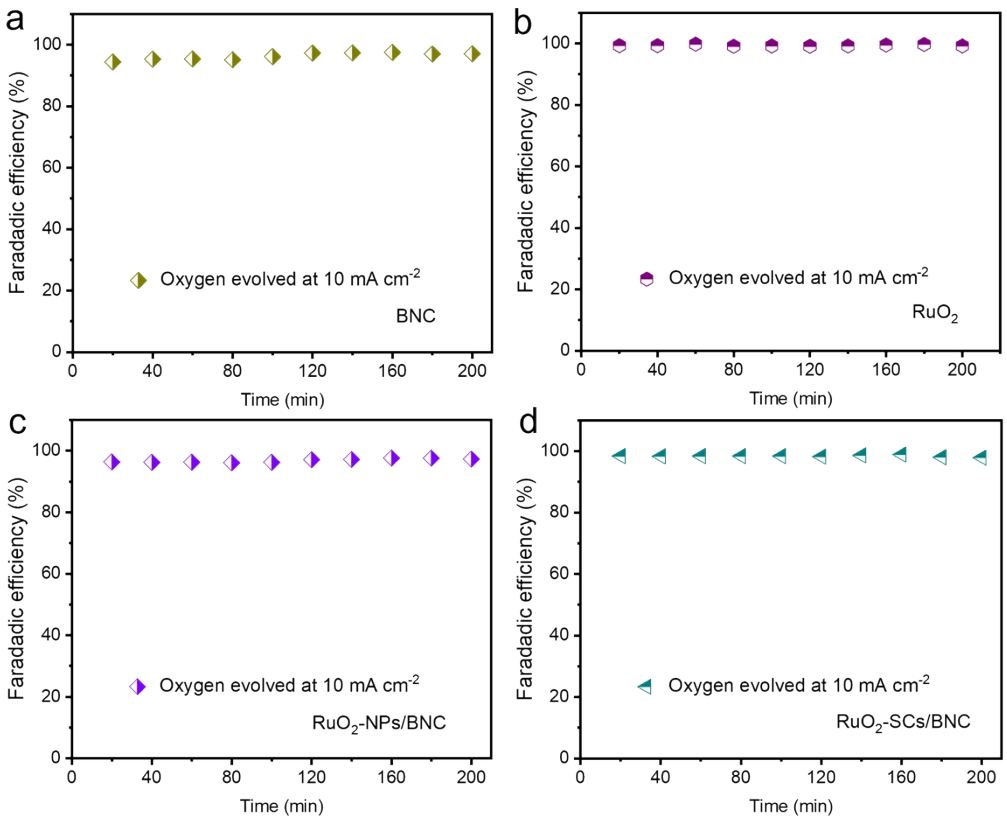

Figure S13. The FEs of O_2 production by (a) BNC, (b) RuO_2, (c) RuO_2-NPs/BNC and (d) RuO_2-SCs/BNC at different reaction times at a current density of 10 mA cm^{-2}.

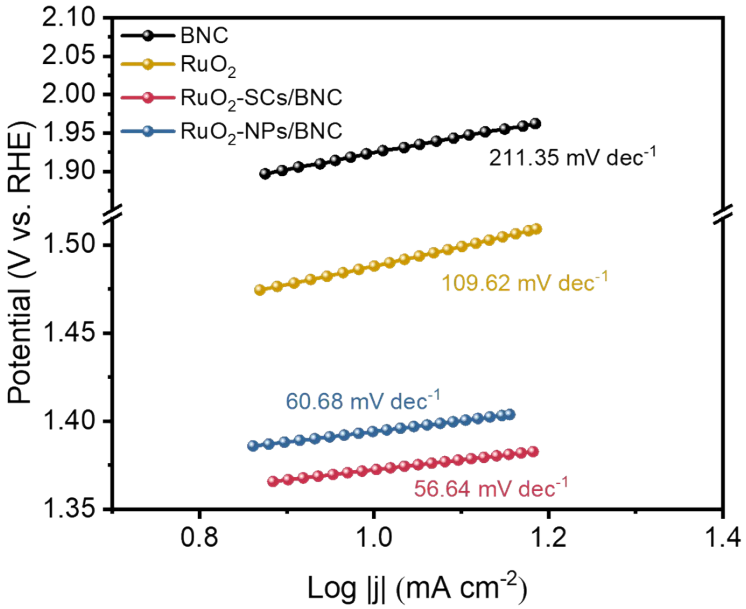

Figure S14. Tafel plots of BNC, RuO_2, RuO_2-SCs/BNC and RuO_2-NPs/BNC calculated from the iR-corrected polarization curves.

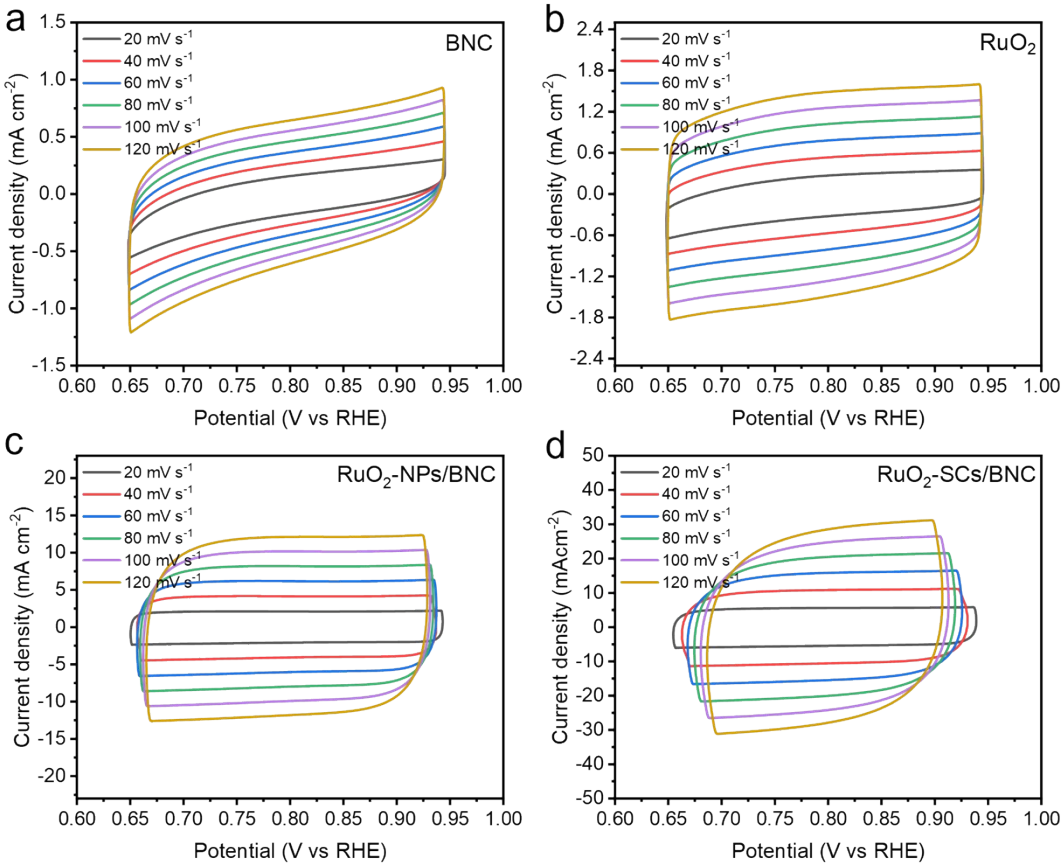

Figure S15. ECSA of (a) BNC, (b) RuO_2, (c) RuO_2-NPs/BNC and (d) RuO_2-SCs/BNC. CV profiles of different catalysts were collected from the non-Faradaic region with the scan rate of 20, 40, 60, 80, 100 and 120 mV s^{-1}.

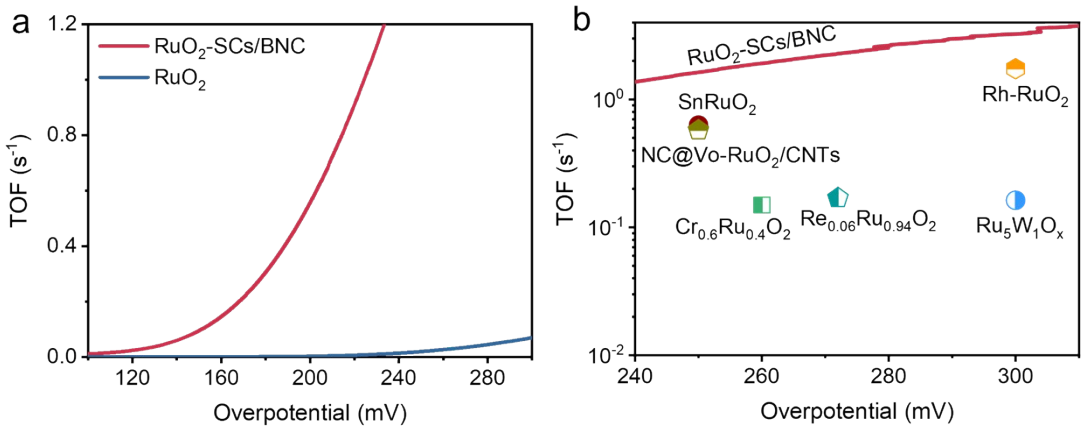

Figure S16. (a) TOFs of RuO_2 and RuO_2-SCs/BNC for OER obtained based on the overall amounts of Ru sites on the electrode. (b) TOF comparison of Ru sites in RuO_2-SCs/BNC with reported Ru-based PEMWE anode catalysts.

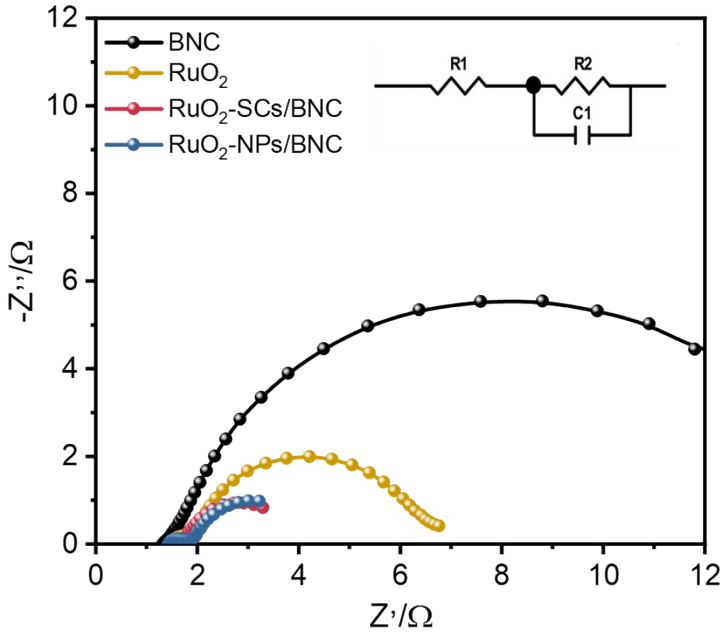

Figure S17. Nyquist plots of BNC, RuO_2, RuO_2-SCs/BNC and RuO_2-NPs/BNC for OER. The inset shows equivalent circuit models for OER.

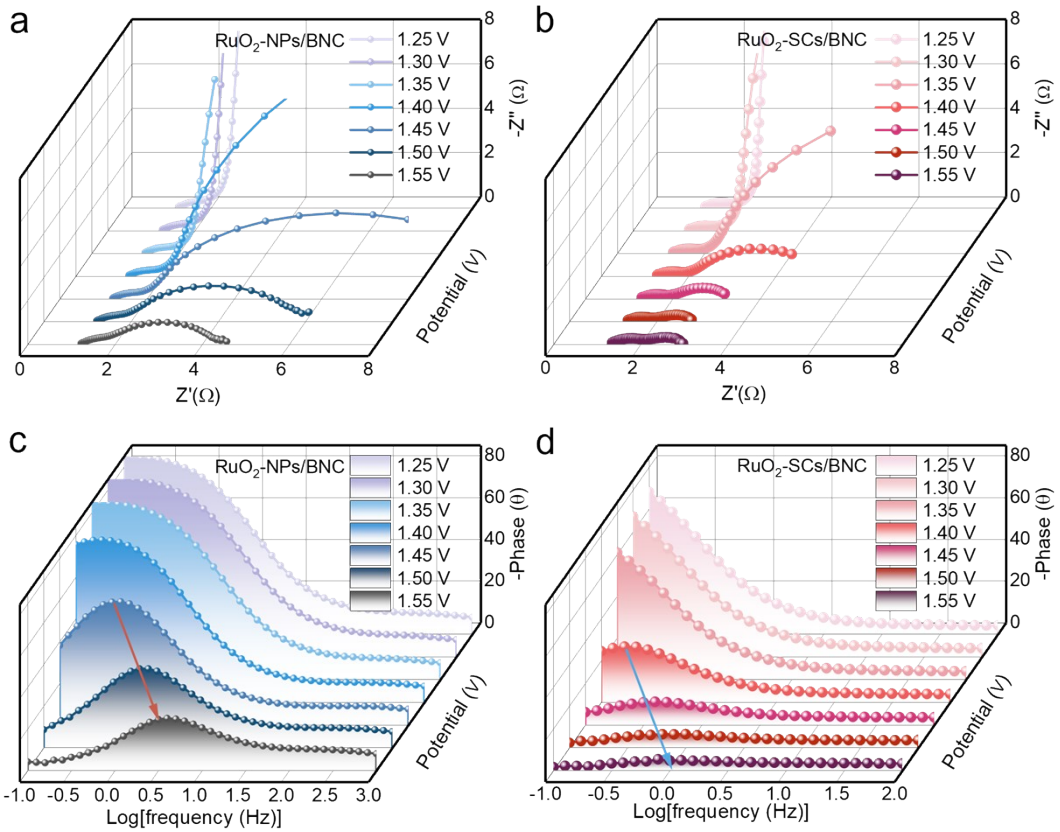

Figure S18. In situ EIS of (a) RuO_2-NPs/BNC and (b) RuO_2-SCs/BNC at the different potentials. The corresponding Bode plots of (c) RuO_2-NPs/BNC and (d) RuO_2-SCs/BNC measured at different potentials (phase angle relaxation as a function of frequency). All potentials were normalized against the reversible hydrogen electrode.

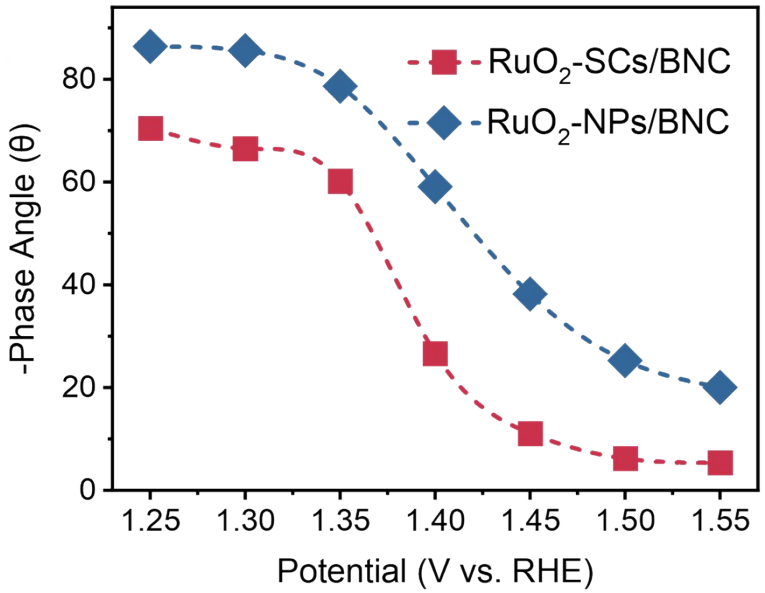

Figure S19. Comparison of phase angles of RuO_2-SCs/BNC and RuO_2-NPs/BNC at different potentials.

The phase angle changes of RuO_2-SCs/BNC and RuO_2-NPs/BNC indicated a large electron transfer resistance. In contrast, the observed phase peak angle of RuO_2-SCs/BNC in the low-frequency region was smaller, indicating that the interaction between the catalyst and the electrolyte interface enhanced the charge transfer process and thus improved the kinetics of OER. In addition, the charge transfer resistance of the RuO_2-SCs/BNC electrocatalyst was lower than that of RuO_2-NPs/BNC, which indicated that the adsorption of oxygen-containing active species had a faster kinetic rate in the acidic OER process.

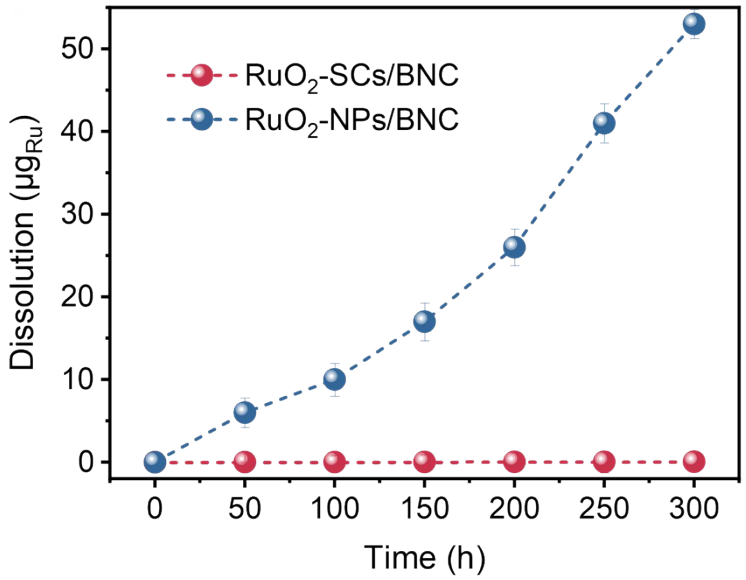

Figure S20. The dissolution of Ru in RuO_2-SCs/BNC and RuO_2-NPs/BNC collected at different times during the OER stability test.

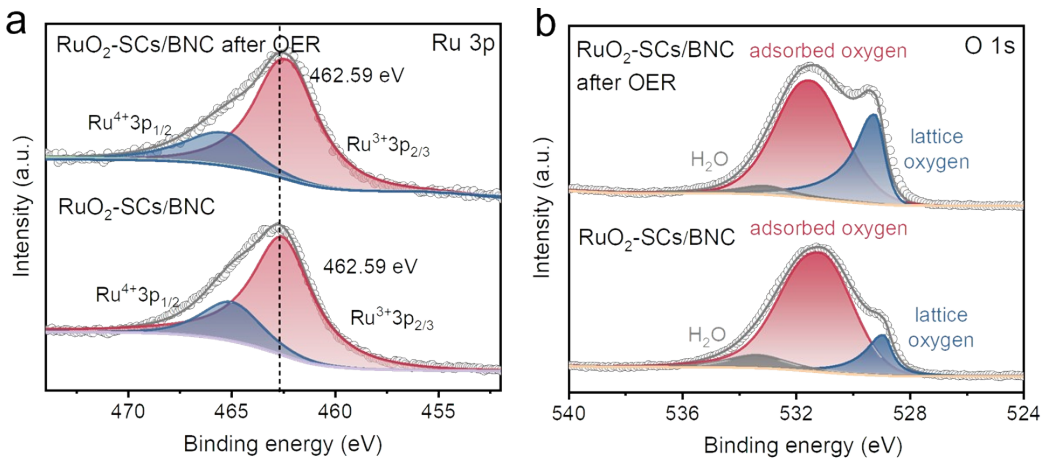

Figure S21. XPS surveys of (a) Ru 3p and (b) O 1s regions for RuO_2-SCs/BNC and RuO_2-NPs/BNC before and after stability test.

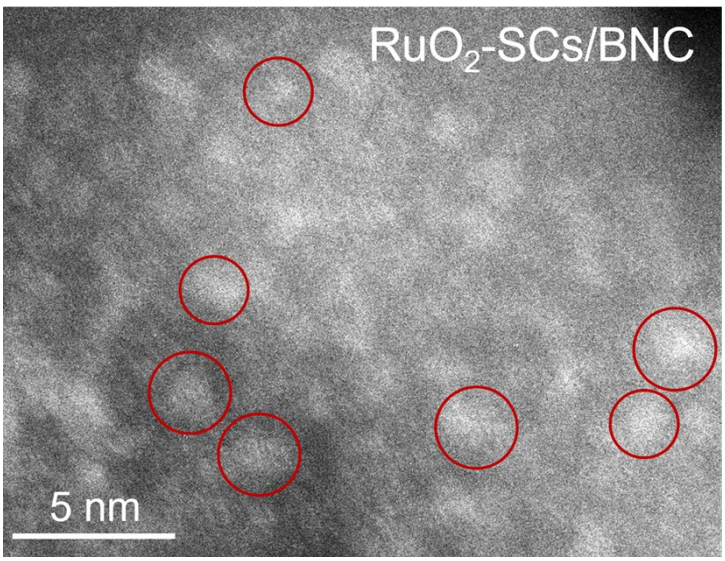

Figure S22. TEM image of RuO_2-SCs/BNC after the stability test for acidic OER**.**

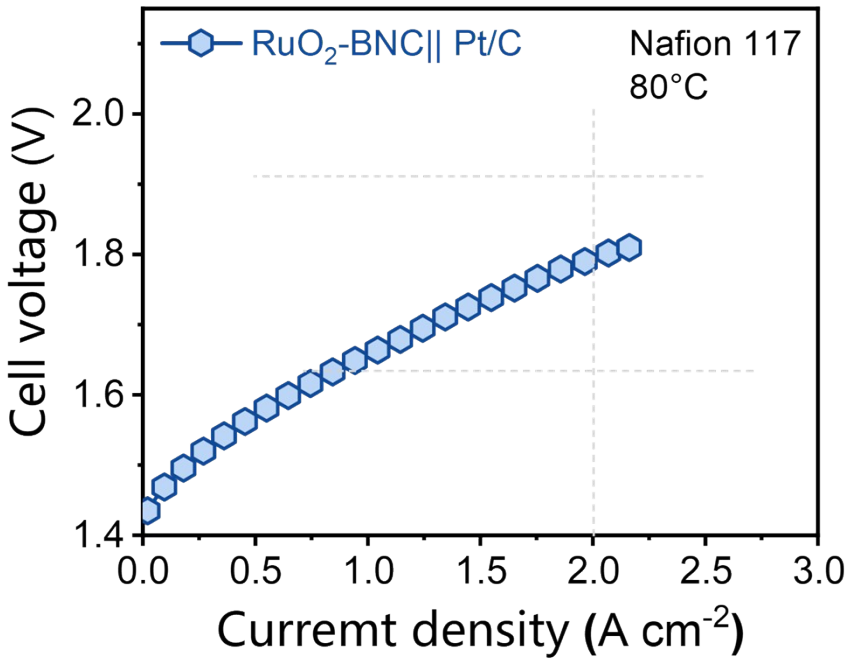

Figure S23. The I-V curve for PEMWE using RuO_2-SCs/BNC as the anodic catalyst and Pt/C as the cathodic catalyst.

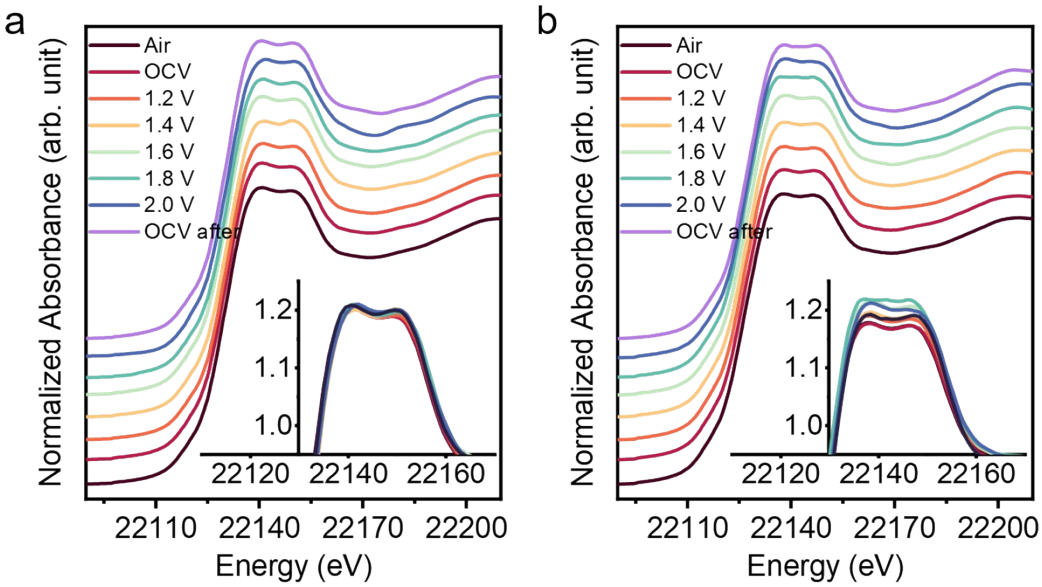

Figure S24. Operando XAFS of (a) RuO_2-SCs/BNC and (b) RuO_2-NPs/BNC with applied bias rise from 1.2 to 2.0 V versus RHE.

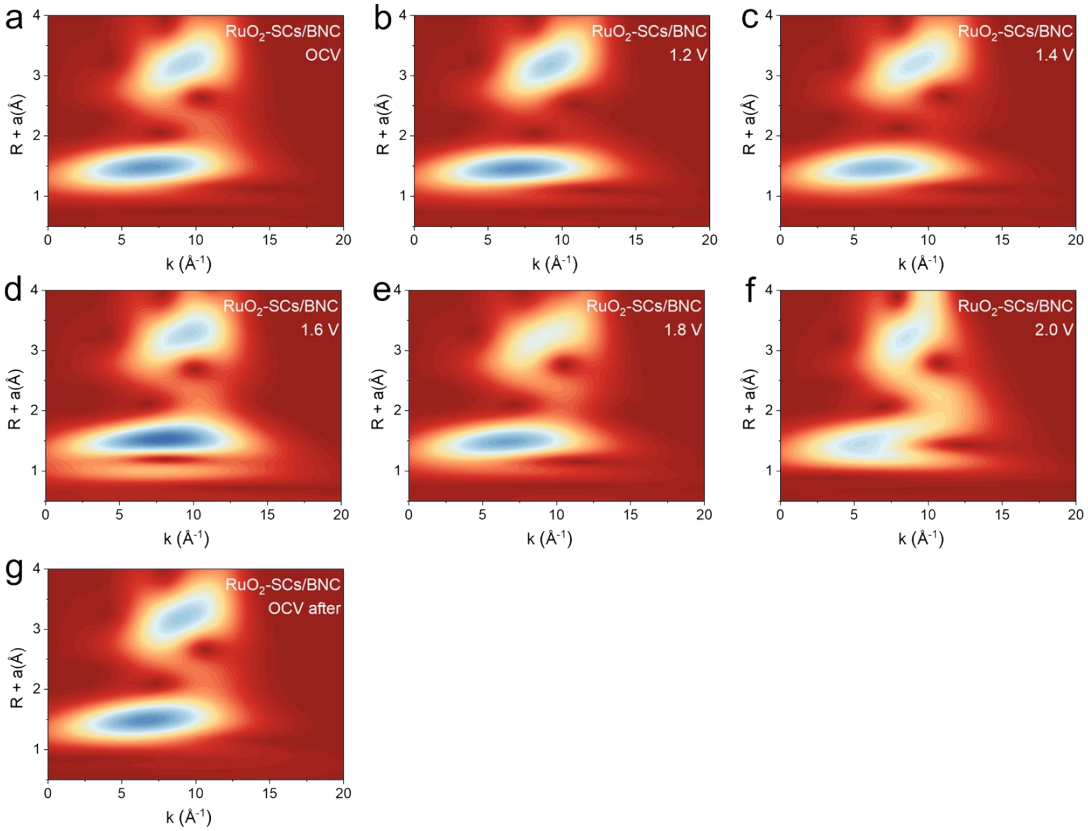

Figure S25. WT-EXAFS of RuO_2-SCs/BNC at the Ru K-edge measured at different potentials.

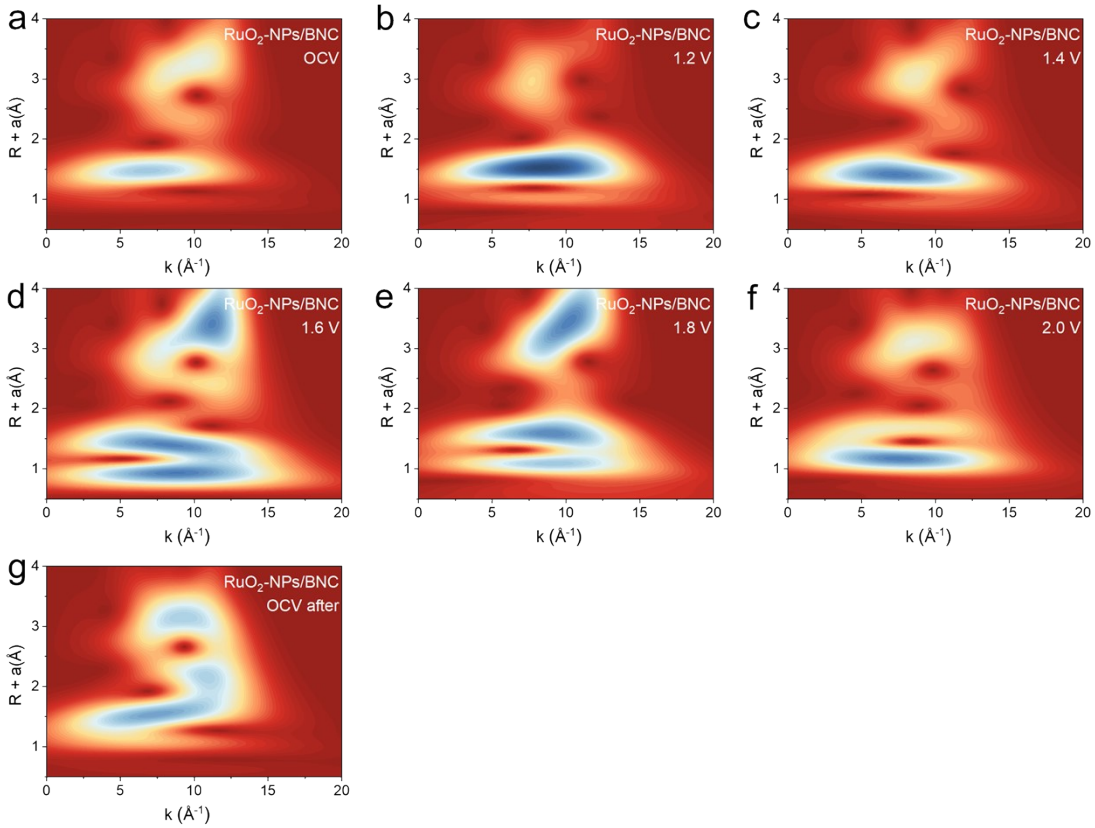

Figure S26. WT-EXAFS of RuO_2-NPs/BNC at the Ru K-edge measured at different potentials.

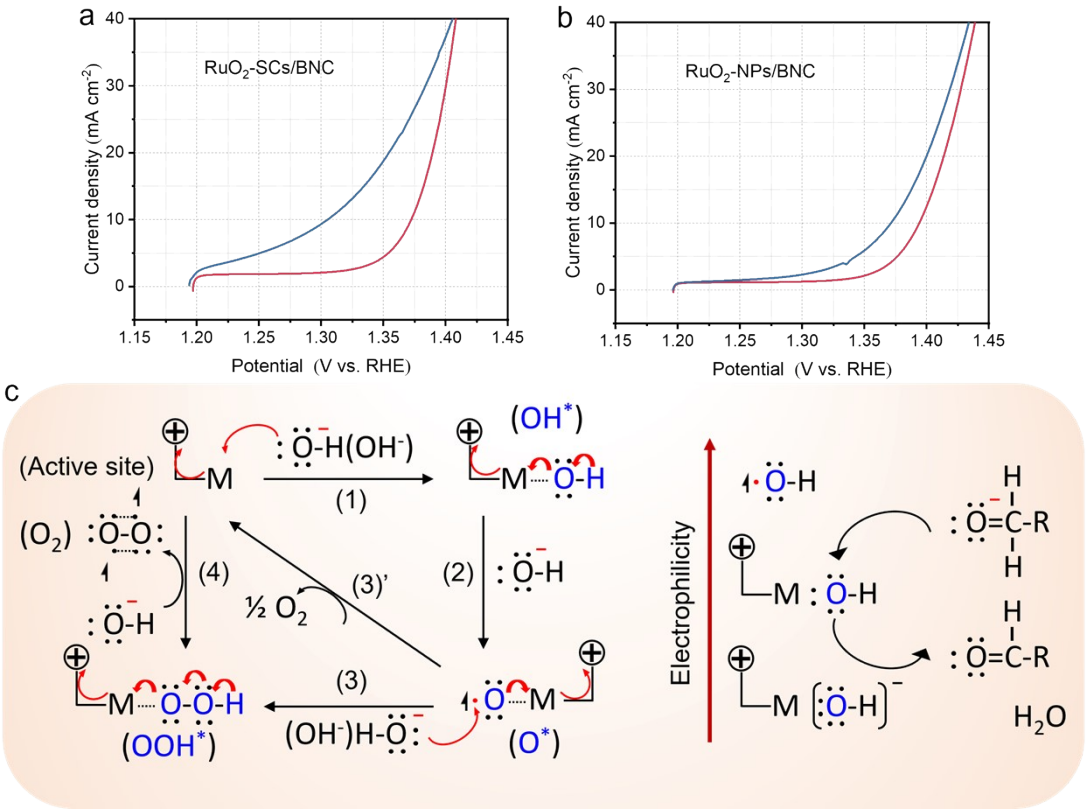

Figure S27. LSV plots of (a) RuO_2-SCs/BNC and (b) RuO_2-NPs/BNC with and without methanol. (c) Electron transfer mechanism in OER O atom redox and probing OH* with nucleophiles.

For Figure S26 (c), the left panel is the consumption of oxygen valence electrons during the OER catalytic cycle. Red curved arrows indicate the direction of electron transfer. Short dashed lines denote chemical bonds between intermediates and catalytic sites. The right panel is the schematic illustration of the principle for detecting OH* intermediates, showing the reaction of methanol oxidation with OH* as an example.

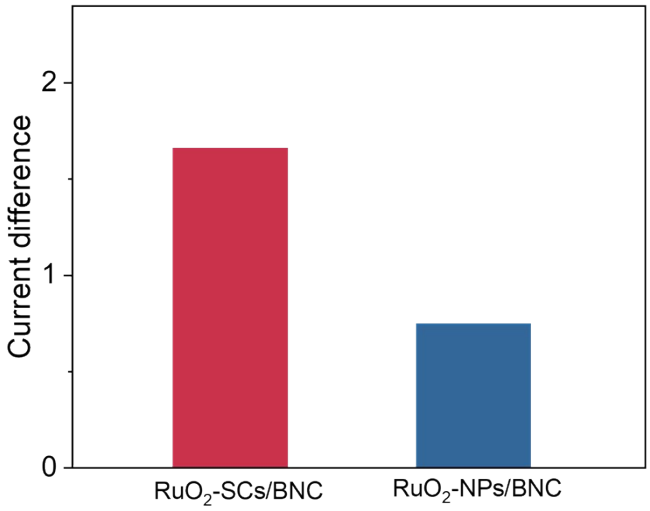

Figure 28. Current difference between the polarization curves in 0.5 M H_2SO_4 solution with and without 0.1 M methanol for RuO_2-SCs/BNC and RuO_2-NPs/BNC.

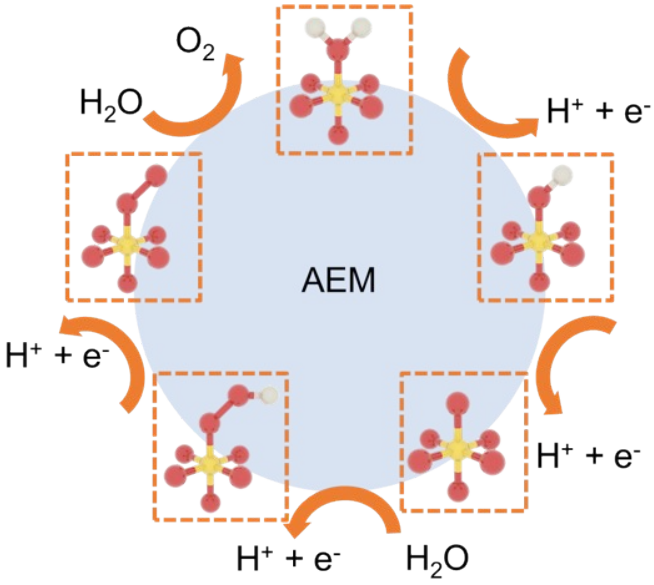

Figure S29. Simplified OER mechanism of the adsorbate evolution mechanism (AEM). (Yellow, red and white balls represent Ru, O and H atoms, respectively)

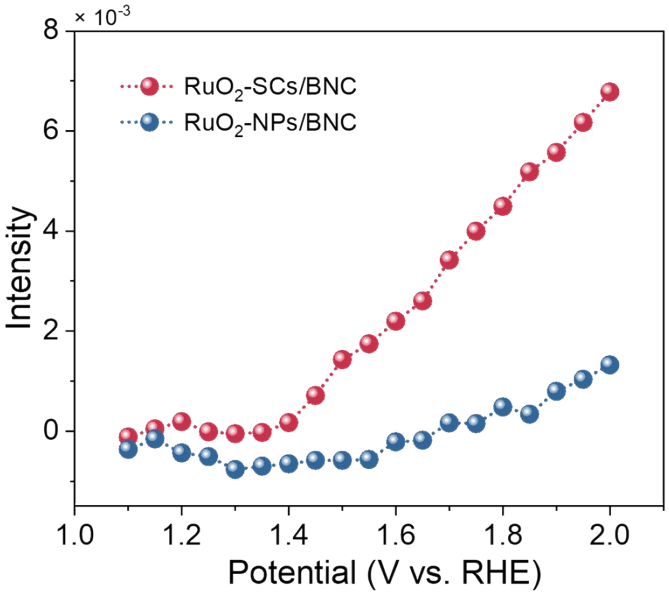

Figure S30. Summary of the *OOH intensity of RuO_2-SCs/BNC and RuO_2-NPs/BNC achieved from in situ FTIR at various potentials without ESCA normalization.

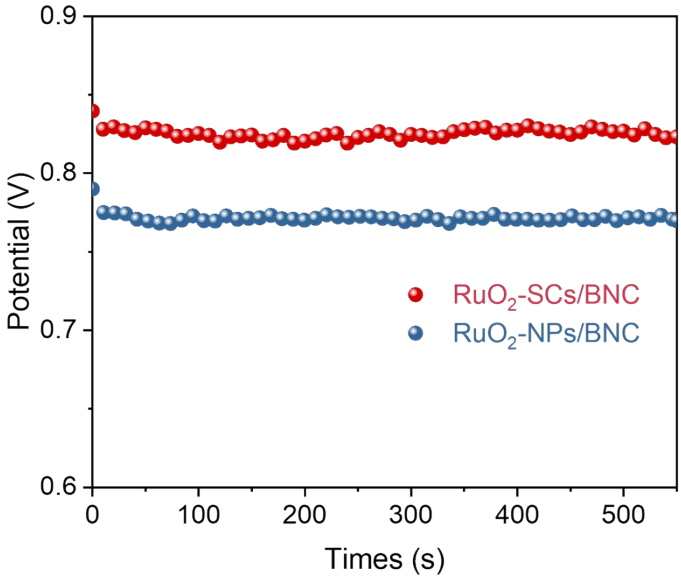

Figure S31. Open-circuit voltage (OCV) measurements of RuO_2-SCs/BNC and RuO_2-NPs/BNC (measured with an electrochemical workstation).

The OCV measurement results provided direct evidence for the enhancement of the compact layer potential. As shown in Figure S29, the OCP value of the RuO_2-SCs/BNC electrode after reaching a steady state was significantly higher than that of the RuO_2-NPs/BNC electrode. A higher OCP indicates that the electrode can effectively increase its intrinsic potential, and this change inevitably leads to an increased number of ions adsorbed on the electrode surface and a stronger interfacial electric field at the same working potential, i.e., a higher compact layer potential. Thus, the RuO_2-SCs/BNC electrode indeed realizes the optimization of the surficial electric field.

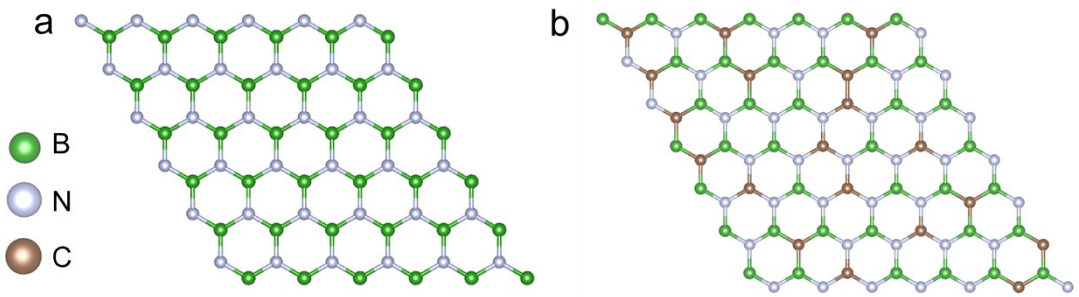

Figure S32. The DFT models of (a) h-BN and (b) BNC. B, N and C atoms are colored green, grey and blown, respectively.

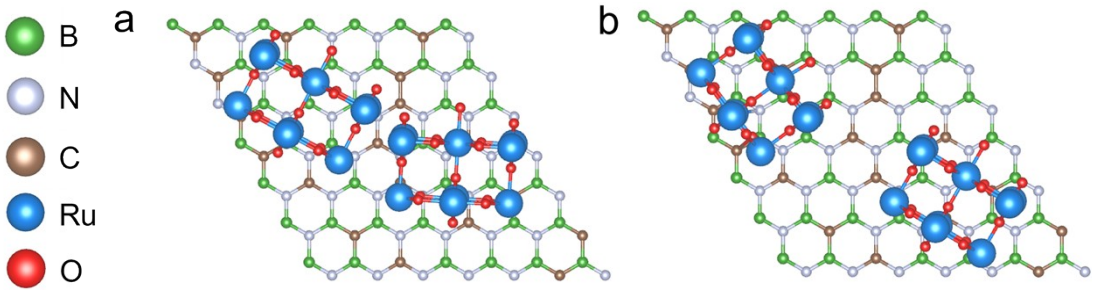

Figure S33. The DFT models of (a) H-RuO_2-BNC and (B) L-RuO_2-BNC. B, N, C, Ru and O atoms are colored green, grey, blown, blue and red, respectively.

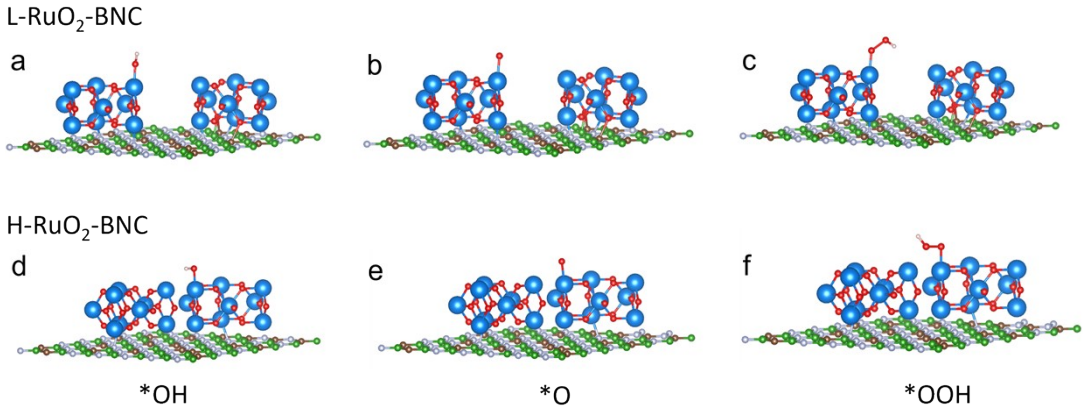

Figure S34. Schematic of different Obri sites on the (a-c) L-RuO_2-BNC and (d-e) H-RuO_2-BNC, according to the DFT investigation of hydrogen adsorption. OER started from the chemisorption of H_2O, followed by generating OH*, O*, OOH* and O_2 species.

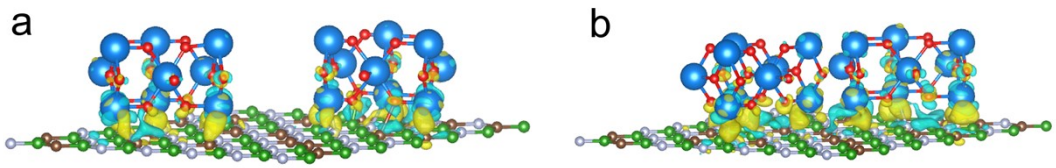

L-RuO_2-BNC (0.511 e) H-RuO_2-BNC (0.873 e)

Figure S35. The calculated charge density difference for (a) L-RuO_2-BNC and (b) H-RuO_2-BNC between RuO_2 with different densities anchored on the BNC support. Yellow and blue regions represent electron accumulation and depletion, respectively.

Table S1. Comparison of the activity and stability of RuO_2-SCs/BNC with reported Ru-based OER catalysts (j = 10 mA cm^{-2}).

	Samples	Overpotential (mV)	Stability (h)	Substrate	Reference
1	**RuO_2-SCs/BNC**	**142**	**6300**	**Carbon paper**	**This work**
2	Ni-RuO_2	214	200	Glassy carbon	Nat. Mater. 2023, 22, 100.
3	Ru/MnO_2	161	200	Glassy carbon	Nat. Catal. 2021, 4, 1012.
4	Na-RuO_2	200	1800	Carbon fiber paper	J. Am. Chem. Soc. 2025, 147, 10446.
5	Ru/MnO_2	179	1000	Carbon paper	J. Am. Chem. Soc. 2025, 147, 18295.
6	$Mn_{(SA)}$/RuO_2	213	1000	Glassy carbon	J. Am. Chem. Soc. 2025, 147, 17839.
7	Co-Ru@RuO_2	203	420	Glassy carbon	J. Am. Chem. Soc. 2025, 147, 8720.
8	Ru-RuO_2-SN	165	1400	Glassy carbon	J. Am. Chem. Soc. 2025, 147, 13775.
9	PtRu-Co_3O_4	143	1000	Carbon fiber paper	J. Am. Chem. Soc. 2024, 146, 28728.
10	$Ru_{0.6}Cr_{0.2}Ti_{0.2}O_2$	190	1100	Carbon paper	J. Am. Chem. Soc. 2024, 146, 15740.
11	$Ru_{0.8}Sb_{0.2}O_2$	160	1100	Carbon paper	J. Am. Chem. Soc. 2024, 146, 23146.
12	RuO_2-HEAE	214	1500	Carbon paper	Nat. Commun. 2025, 16, 6894.
13	Pt-RuO_2	215	1500	Glassy carbon	Nat. Commun. 2025, 16, 6217.
14	$Ta_{0.1}Sr_{0.1}Ru_{0.8}O_{2-x}$	166	1000	Carbon paper	Nat. Commun., 2025, 16, 1717.
15	GB-V-RuO_2	159	760	Glassy carbon and carbon paper	Nat. Commun, 2025, 16, 4482.
16	$N_{0.1}M_{0.1}RO$	207	200	Carbon fiber paper	Nat. Commun. 2025, 16, 4583.
17	COF-205-Ru	210	280	Glassy carbon	Nat. Commun. 2024, 15, 5419.
18	$Mn_{0.2}RuO_2$	188	150	Glassy carbon	Nat. Commun. 2024, 15, 8089.
19	Er-RuO_x	200	200	Carbon paper	Nat. Commun. 2024, 15, 4974.
20	Si-RuO_2-0.1	226	800	Glassy carbon	Nat. Commun. 2024, 15, 2501.
21	a-RuO_x-l	215	300	Carbon paper	Angew. Chem. Int. Ed. 2025, 64, e202504876.
22	Ru/RuO_2	183	600	Glassy carbon	Angew. Chem. Int. Ed. 2025, 64, e202503733.
23	Vn-RuO_2	227	1050	Glassy carbon	Angew. Chem. Int. Ed. 2025, 64, e202413657.
24	Ga-RuO_x	190	100	Carbon paper	Angew. Chem. Int. Ed. 2025, 64, e202505908.
25	$RuS_{0.45}O_x$	160	1000	Glassy carbon	Angew. Chem. Int. Ed. 2025, 64, e202420848.
26	$MnRuO_x$	231	700	Carbon paper	Angew. Chem. Int. Ed. 2024, 63, e202405641.

27	In-RuO_2/G	187	100	Glassy carbon	Angew. Chem. Int. Ed. 2024, 63, e202316903.
28	$RuSnO_x$	184	150	Carbon cloth	Angew. Chem. Int. Ed. 2024, 63, e202316029.
29	C, Ta-RuO_2	171	1300	Glassy carbon	Adv. Mater. 2025, 37, 2503354.
30	m-RudO_2	230	100	Carbon paper	Adv. Mater. 2024, 36, 2404213.
31	RuFe@CF	188	620	Activated carbon felt	Adv. Mater. 2024, 36, 2312369.
32	$H_{3.8}Ir_{1-x}Ru_xO_4$	255	1100	Carbon paper	Adv. Mater. 2024, 36, 2407394.
33	$Ru_{0.5}Mn_{0.5}O_2$	166	2500	Glassy carbon	Energy Environ. Sci. 2025,18, 3352.
34	Ru/TiO_x	237	160	Carbon fiber paper	ACS Catal. 2025, 15, 768.
35	Ce-RuO_{2-x}	215	300	Glassy carbon	Chem. Catal. 2024, 4, 101035.